RESEARCH ARTICLE

Complex rupture process on the conjugate fault system of the 2014 Mw 6.2 Thailand earthquake

Tira Tadapansawut[1]* , Yuji Yagi[2]*, Ryo Okuwaki[2,3,4], Shinji Yamashita[5] and Kousuke Shimizu[5]

Abstract

A moment magnitude 6.2 crustal earthquake occurred in northern Thailand on May 5, 2014, and its aftershocks exhibit several lineaments with conjugate pattern, involving geometric complexity in a multi-segmented fault system of the Phayao Fault Zone. However, a relationship between those geometric complexities and the rupture evolution of the 2014 Thailand earthquake is still elusive, which is critical to understand complex nature of the earthquake physics and to assess the hazard. Here, we elaborated the newly developed potency density tensor inversion method, used it to invert the globally observed teleseismic P waveforms, and estimated the spatiotemporal distribution of both the slip and the fault geometry. We found the complex rupture evolution consisting of two rupture episodes along a conjugated strike-slip fault system that comprises two distinct fault planes. The first episode originated at the hypocenter and the rupture propagated south along the north–northeast to south–southwest fault plane. The second episode was triggered at around 5 km north from the epicenter, and the rupture propagated along the east–northeast to west–southwest fault plane and terminated at the west end of the source area at 5 s hypocentral time. Our work demonstrates that our potency density tensor inversion can be applied to the smaller-scale magnitude-6 class earthquakes, and it resolves the complex rupture process controlled by the underlying geometric complexity in the fault system.

Keywords: 2014 Thailand earthquake, Complex rupture process, Teleseismic P waveform potency density tensor inversion, Conjugate fault

1 Introduction

The seismicity of Thailand is relatively low: less than 10 earthquakes with a magnitude greater than 5 have been registered since the 1970s (ISC 2021) (Fig. 1). Although situated in a low seismicity zone, Thailand is surrounded by major active faults, such as the Sagaing Fault in Myanmar and the major Aliao Shan-Red River fault north of Thailand (Morley et al. 2011) (Fig. 1). These faults are
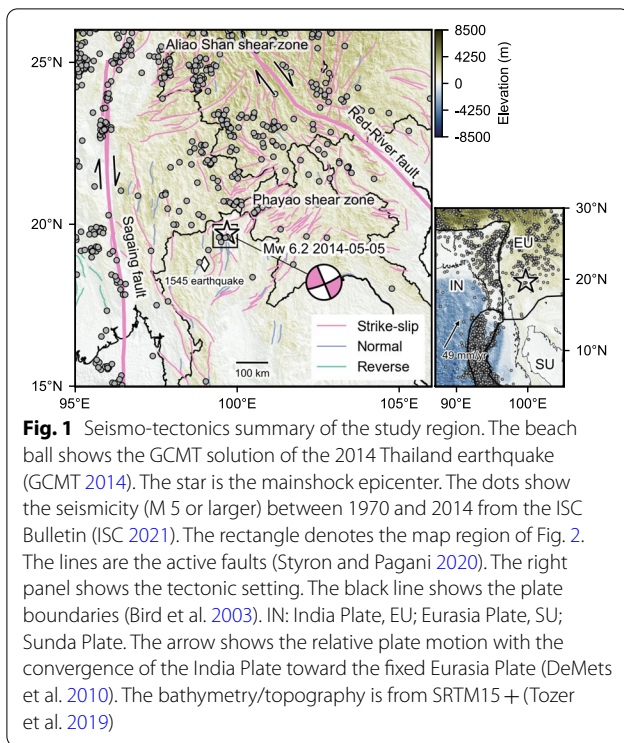
subject to a progressive clockwise strain rotation caused by the motions induced by the escape tectonics from the Tibetan Plateau to SE Asia and the Sumatra–Andaman subduction zone (Huchon et al. 1994; Leloup et al. 2001; Morley 2002, 2007; Morley et al. 2011). Thailand has complex geological structures that include multiple active fault zones (Morley 2002; Morley et al. 2011) (Fig. 1). Many active fault zones in Thailand are part of a strike-slip fault system trending northeast–southwest and northwest–southeast (Charusiri and Pum-Im 2009; Morley et al. 2011). These trends are a result of the development of the major Cenozoic rift basin that is subject to a north–south compression and east–west extension. Geological records suggest that there is historical seismicity since the Late Quaternary in the northern part

*Correspondence: tira.tadapansawut@gmail.com; yagi-y@geol.tsukuba.ac.jp

[1] Graduate School of Life and Environmental Sciences, University of Tsukuba, Tsukuba, Ibaraki 305-8572, Japan
[2] Faculty of Life and Environmental Sciences, University of Tsukuba, Tsukuba, Ibaraki 305-8572, Japan
Full list of author information is available at the end of the article

Fig. 1 Seismo-tectonics summary of the study region. The beach ball shows the GCMT solution of the 2014 Thailand earthquake (GCMT 2014). The star is the mainshock epicenter. The dots show the seismicity (M 5 or larger) between 1970 and 2014 from the ISC Bulletin (ISC 2021). The rectangle denotes the map region of Fig. 2. The lines are the active faults (Styron and Pagani 2020). The right panel shows the tectonic setting. The black line shows the plate boundaries (Bird et al. 2003). IN: India Plate, EU; Eurasia Plate, SU; Sunda Plate. The arrow shows the relative plate motion with the convergence of the India Plate toward the fixed Eurasia Plate (DeMets et al. 2010). The bathymetry/topography is from SRTM15 + (Tozer et al. 2019)

Fig. 2 The study area of the 2014 Thailand earthquake. The open star shows the mainshock hypocenter. The large beach ball shows the GCMT solution of the 2014 Thailand earthquake (Dziewonski et al. 1981; Ekström et al. 2012). The small beach balls show the focal mechanism of the relocated aftershocks with the moment magnitude larger than 4.2 (Pananont et al. 2017). The pink lines highlight the aftershock lineations of the NSTA and EWTA. The black lines are the active faults of the Phayao Fault Zone (DMR 2016; Kanthiya et al. 2019): MLF; Mae Lao fault, PF; Phan fault, MSF; Mae Suai fault, MSBF; Mae Suai Boundary fault, and MJF; Mae Jai fault. The topography is from SRTM15 + (Tozer et al. 2019). The lower panel shows the cross section of the aftershocks projected along the EWTA within – 4/+ 10 km width across the projected track. The dashed line denotes the projected location of the hypocenter. The bottom panel shows the cross section of the aftershocks projected along the NSTA within ± 3 km width across the projected track. The open star denotes the mainshock hypocenter (Pananont et al. 2017)

of Thailand associated with the active fault zones (Fenton et al. 2003; Pailoplee and Charusiri 2016). One of the largest historical earthquakes in 1545 collapsed an immense pagoda in Wat Chedi Luang temple in Chiang Mai province (Kázmér et al. 2011) (Fig. 1).

The largest recent earthquake in Thailand, which is a focus of this study, had a moment magnitude (M_W) 6.2 and occurred in the northern part of the country on 5 May 2014 (GCMT 2014; Pananont et al. 2017). The 2014 Thailand earthquake affected 7 provinces, damaged more than 7000 buildings, and caused 1 death and 107 injuries (Lhamphoonsup et al. 2014; Wechbunthung 2014; Wiwegwin and Kosuwan 2014). The geological field survey was taken 54 days after the earthquake, and they show that there is no direct evidence of the surface rupture. However, they found many secondary damage effects from the ground shacking such the liquefaction concentrating near the epicenter and the ground cracks which show the pattern toward south and southwest from the epicenter (Pananont et al. 2017). The analyses of synthetic aperture radar (SAR) images were hampered by the regional dense vegetation, which prevented the instrument from measuring co-seismic surface deformation, including the surface rupture trace around the source region (Nardkulpat et al. 2017).

The source region is situated in the Phayao Fault Zone (PFZ) (Fenton et al. 2003; Pailoplee et al. 2009), and the epicenter of the 2014 Thailand earthquake (Noisagool
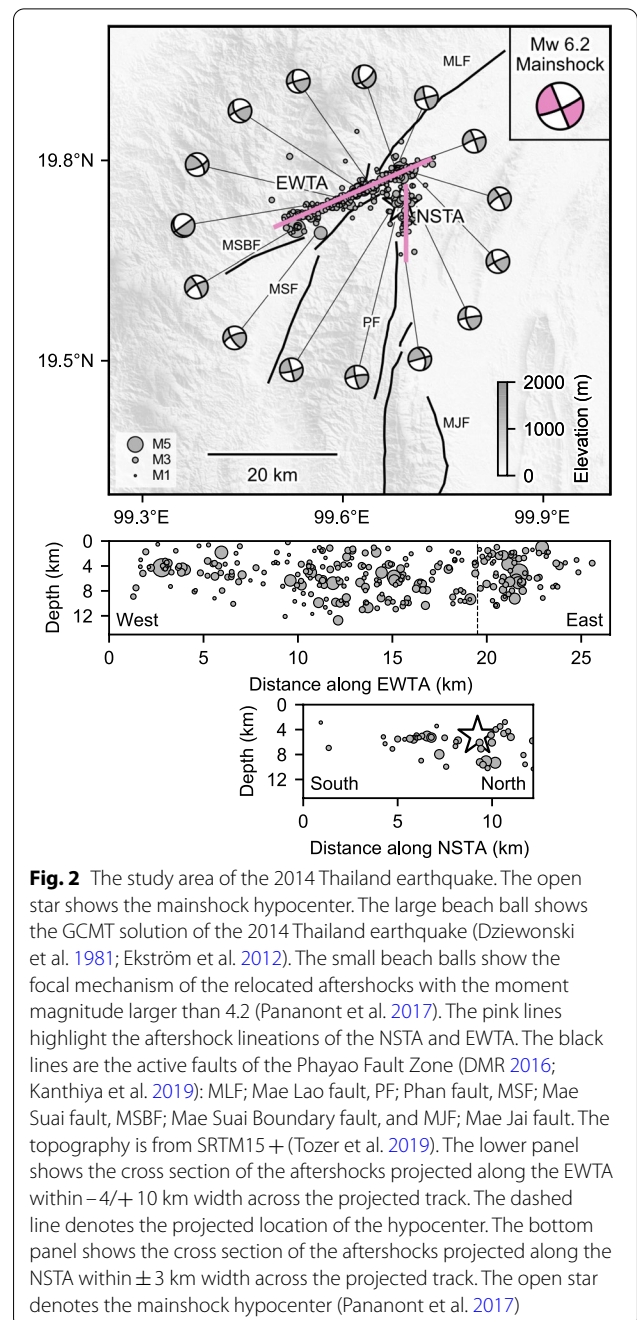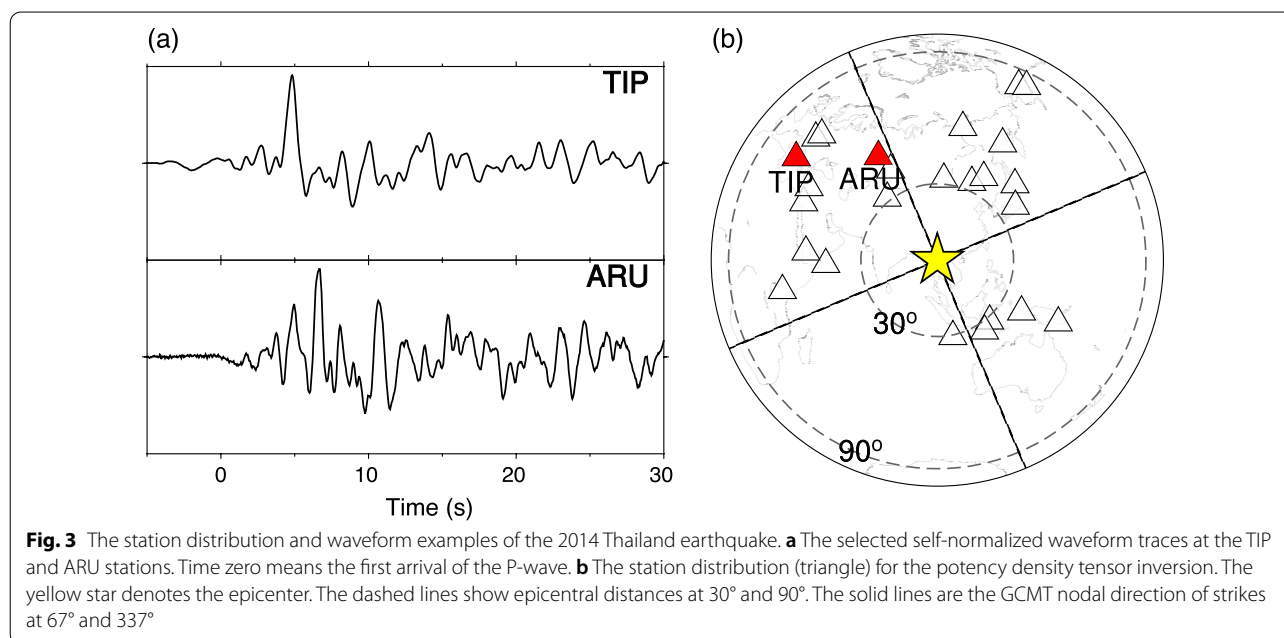
et al. 2016; Pananont et al. 2017; TMD 2014; USGS 2014) is located at the transition zone within the conjugated fault system of two major active strike-slip faults: the Mae Lao Fault (MLF) trending ENE-WSW and the Phan Fault (PF) trending N-S (Noisagool et al. 2016; Pananont et al. 2017) (Fig. 2). A relocated hypocenter of the 2014 Thailand earthquake determined by the double-difference algorithm HypoDD (Pananont et al. 2017) is located at 19.733° N and 99.689° E with a 5.2 km hypocentral depth

that is between the middle of the MLF and the top of the PF (Fig. 2). The centroid moment tensor solution shows the nodal planes orienting NNW-SSE and ENE-WSW with M_W 6.2 (GCMT 2014). The relocated aftershocks during the first week from the HypoDD (Pananont et al. 2017) can be divided into two major groups: the N-S trending aftershocks (NSTA) and the ENE-WSW trending aftershocks (EWTA) (Fig. 2). The aftershocks focus within 4–6 km depth range at the western edge of the EWTA, whereas the aftershocks along the NSTA dominate 2–10 km deep around the hypocenter (Pananont et al. 2017). The regional moment tensor solutions of the aftershocks (Pananont et al. 2017) are located along the NSTA and EWTA, with their strike directions aligned with the trends of the NSTA and EWTA (Fig. 2).

The regional moment tensor solutions of the mainshock and the aftershocks (Noisagool et al. 2016) show that the principal compressive stress orientation is NNE-SSW (N18°E) that is consistent with the regional stress orientation in northern Thailand (Heidbach et al. 2016; Noisagool et al. 2016; Simons et al. 2007). The high shear stress zone is related to the strike orientation of the active MLF that is close to the EWTA: N30°E–N50°E. This high shear stress zone contributes to the initiation of slip based on Mohr–Coulomb failure criteria (Noisagool et al. 2016). Pananont et al. (2017) studied the aftershocks sequence occurring within hours by analyzing the changes in the stress field due to the rupture, for which they computed the Coulomb stress changes: they suggested that the mainshock occurred on the right-lateral faulting along the NSTA. They argued that the complex

rupture process has produced the complicated pattern of the aftershock distribution. However, the source mechanism of the 2014 Thailand earthquake has not been clearly understood; whether the rupture evolves along the apparent conjugate fault system is inferred from the aftershock distribution. The detailed imaging of the source process of the 2014 Thailand earthquake should be a critical basis to illuminate the causative relationship between the rupture evolution and the geometric complexity in the fault system for the smaller-scale, *M*6-class earthquake, which has been difficult to investigate in a means of finite-fault inversion.

A possibility for a complex fault geometry can be expected from a simple observation of the teleseismic waveforms. If an earthquake occurs along a single, simple fault plane, the teleseismic waveforms at stations within the same quadrant of the focal mechanism are expected to be similar without being contaminated by too many reflection/refraction phases. In the case of the 2014 Thailand earthquake, the stations TIP and ARU are in the same quadrant of the GCMT moment tensor solution (Fig. 3). The waveforms of the TIP and ARU stations show the different waveform shape and amplitude, which is unexpected if the earthquake rupture propagates along a single flat plane with a constant slip vector (e.g., Tadapansawut et al. 2021). This may imply that the mainshock mechanism may involve geometric complexity. We note that the difference in data may also arise from small variations in the travel path, which can be associated with polarity changes of P-wave and may include more complexity in the seismogram. In addition, the aftershock distribution with two

Fig. 3 The station distribution and waveform examples of the 2014 Thailand earthquake. **a** The selected self-normalized waveform traces at the TIP and ARU stations. Time zero means the first arrival of the P-wave. **b** The station distribution (triangle) for the potency density tensor inversion. The yellow star denotes the epicenter. The dashed lines show epicentral distances at 30° and 90°. The solid lines are the GCMT nodal direction of strikes at 67° and 337°

major trends of the NSTA and EWTA (Fig. 2) also suggests the complexity of fault geometry of the mainshock. To resolve the possible complex fault geometry, we apply a new framework of the potency density tensor inversion algorithm for teleseismic body waveforms (Yamashita et al. 2021). We introduce a relative weight smoothness constraint that is proportional to the components of each basis moment tensor (Kikuchi and Kanamori 1991) into the potency density tensor inversion of Shimizu et al., (2020) which can mitigate the effect of the modeling errors originating from the uncertainty of Green's function (Yagi and Fukahata 2011) as well as the uncertainty of fault geometry (Ragon et al. 2018) (see details in the Method section). This method can simultaneously estimate the distribution of the focal mechanism and the slip along the assumed model plane; it enables the reconstruction of complex rupture processes, including those occurring along faults containing fault bends and those consisting of multiple subevents, without a priori assumption of the fault geometry (Tadapansawut et al. 2021; Yamashita et al. 2021). The improved potency density tensor inversion framework has been applied to large earthquakes such as the 2020 M_W 7.7 Caribbean earthquake (Tadapansawut et al. 2021) and the 2018 M_W 7.9 Gulf of Alaska earthquake (Yamashita et al. 2021), but it has never been applied to smaller-scale $M6$-class earthquakes like the 2014 Thailand earthquake. In this study, we apply the potency density tensor inversion method to the teleseismic body waves of the 2014 Thailand earthquake. We estimate the spatiotemporal distribution of both the slip and the fault geometry. We then discuss the detailed source process of the 2014 Thailand Earthquake, which is controlled by the geometric complexity of the fault system.

2 Method

To construct a rupture model of the 2014 Thailand earthquake, we apply the potency density tensor inversion of Shimizu et al. (2020). The method can estimate the spatiotemporal distribution of the potency-rate density tensor including the fault geometry information along the assumed model plane without a priori fault geometry assumption; it represents the shear-slip vectors with five basis double-couple moment tensor components (Kikuchi and Kanamori 1991). The observation equation is defined as

$$u_j(t) = \sum_{q=1}^{5} \int_S \left(G_{qj}(t,\xi) + \delta G_{qj}(t,\xi) \right) * \dot{D}_q(t,\xi)d\xi + e_{bj}(t)$$

where u_j is the teleseismic waveform at station j. G_{qj} is Green's function for the qth component of the basis double-couple moment tensor at station j, and δG_{qj} is the error of Green's function. $\dot{D}_q$ is the potency-rate density

function for the qth component of the basis double-couple moment tensor at the source location ξ of the assumed model plane (S). e_{bj} is the background Gaussian noise. We introduce the data covariance matrix, which mitigates the effect of the modeling error related to the error of Green's function, following Yagi and Fukahata (2011). This approach makes it possible to evaluate the information from observed data correctly and to obtain a stable solution even under the assumption of a source process model with a high degree of freedom (e.g., Duputel et al. 2014; Shimizu et al. 2020; Yagi and Fukahata 2011).

In order to obtain a stable distribution of the potency-rate density function, we apply smoothing constraints and the strength of the smoothing constraints is objectively evaluated using the Akaike's Bayesian information criterion (ABIC) (Akaike 1980). ABIC can be used to objectively determine the optimal relative weights of information from observed data and prior constraints, thus preventing over-fitting (e.g., Fukahata and Wright 2008; Yabuki and Matsu'ura 1992; Yagi and Fukahata 2008). In the smoothing constraints proposed by Shimizu et al. (2020), the potency-rate density of the dominant basis component becomes smoother than those of the minor components, because of the spatiotemporal smoothing constraint which was introduced by the Gaussian with a same covariance into the potency-rate density function without distinction for all five basis double-couple components (Yamashita et al. 2021). To mitigate this bias due to the smoothing constraints, we apply a new framework of the relative weight smoothness constraint (Tadapansawut et al. 2021; Yamashita et al. 2021): It adds an inverse relative weight parameter $(1/W_q)$ to the standard deviation of each basis component that is proportional to the double-couple component of the GCMT moment tensor solution (Additional file 1: Fig. S1). To avoid the instability of the solution due to the extremely small relative standard deviation, we set the minimum weight smoothness constraint to 5% of the maximum relative standard deviation. We confirmed that slight changes in the minimum weight do not affect the inversion solution through sensitivity tests perturbing the minimum weight to 10% and 20% (Additional file 1: Fig. S2; Text S1). This new framework has been proven efficient for the analyses of the source process of the 2018 Gulf of Alaska earthquake (Yamashita et al. 2021) and the 2020 Caribbean earthquake (Tadapansawut et al. 2021).

Before applying our newly developed inversion method to the real dataset in the following sections, we first evaluate the resolvability of this approach by performing a numerical test using synthetic waveforms based on the dipping planes of conjugate faults, which are akin to the hypothesized fault system of the 2014 Thailand

Tadapansawut *et al. Progress in Earth and Planetary Science*   (2022) 9:26

Page 5 of 13

earthquake (see Numerical test section). The numerical test shows that the inverted solution can well reproduce the input, which suggests that the potency density tensor inversion can resolve complex ruptures even for cases of smaller-scale (*M*6-class) events consisting of multiple rupture segments and with geometric changes in the fault system.

3 Data and model setting

For the analysis of the 2014 Thailand earthquake rupture, we use 25 vertical components of the globally observed teleseismic waveforms (Fig. 3b) obtained from the Global Seismographic Network and the Federation of Digital Seismograph Network provided by Incorporated Research Institutions for Seismology Data Management Center. The data are selected based on signal-to-noise ratio high-enough to distinguish the P-wave arrival and to ensure azimuth coverage (Fig. 3). Although the earthquake magnitude is small, the waveform at the first 10 s can be distinguished from the noise level (Additional file 1: Fig. S3). We manually pick the first arrival of P-wave and convert it into a velocity waveform to remove the instrument response. Then, we resample it at 0.5 s. Following Kikuchi and Kanamori (1991), we calculate Green's function at 0.1 s sampling rate for the components of each basis moment tensor. The finer sampling of Green's function with respect to the observed waveform sampling ensures sufficient resolution for the time shift relating to location of each sub-fault to the hypocenter. After this, we resample Green's function at 0.5 s, which is the waveform sampling rate. The simplified 1-D near-source structure model (Wongwai et al. 2013) is applied to calculate the Haskell propagation matrix for Green's function (Additional file 1: Table S1). The sensitivity of the near-source structure model is evaluated by testing different models (Additional file 1: Fig. S4; Text S1), and we find that the obtained characteristics of the seismic source process can be reproduced using different structure model. The attenuation time constant *t** for the teleseismic P-waveform is about 1 s (Yagi and Fukahata 2011), and the amplitude of the signal below 1 s is very weak, so the signal is not affected by aliasing even if the sampling interval is shorter than 1 s (Additional file 1: Fig. S5). Therefore, following Shimizu et al. (2020), we do not apply a low-pass filter to both the observed waveforms and the theoretical Green's functions to avoid complicating the structure of the observation and modeling errors by applying a low-pass filter to the errors. By adopting this approach, it is possible to construct a seismic source model which can explain the observed data undistorted by the low-pass filter (Additional file 1: Fig. S3). The assumed model plane is confined by the relocated aftershock distribution and covers the NSTA and

EWTA that are the expected rupture fault planes. We set up the horizontal model plane assuming that the variation of slip in the depth direction is negligible; however, such a supposition can produce a very smooth solution that will impair the interpretation of the rupturing path or the fault geometry. This problem is distinct in the conjugate strike-slip fault earthquakes with multiple fault planes because if the model space is wide and covers unnecessary space where the slip is unlikely to occur, then the unnecessary slip is squeezed out from the actual slip due to the smoothing effects. To mitigate this issue, Yamashita et al. (2021) restricted the horizontal model plane only to the aftershock region and obtained a non-rectangular plane; in that way, the rupture propagation is captured in detail and the solution is more stable. We assume the model plane to have a strike of 60° and a dip of 0°. The model plane is a non-rectangular horizontal model plane with a maximum total length of 30 km along the EWTA and 18 km along the NSTA. The sub-fault has a dimension of 2×2 km^2 and lies along the strike and the dip. The moment rate function for each sub-fault is represented as a linear B-spline function with a 0.5 s interval. The total rupture duration is set at 8.0 s. We tested alternative assumptions of the total rupture duration (Additional file 1: Fig. S6; Text S1) and found that 0–5 s is robustly resolved, but later period, e.g., during 5–8 s, is affected by the assumption of total duration. So we here focus our discussion on the robust rupture process during 0–5 s in the following sections. The maximum rupture velocity is set at 3.6 km/s which is equal to the first layer shear wave velocity (V_s) of the simplified structure model (Wongwai et al. 2013) (Additional file 1: Table S1). We tested the sensitivity of the solution against the maximum rupture velocity assumption, where we found that the assumption of rupture velocity does not affect the solution (Additional file 1: Fig. S7; Text S1). As the initial rupture point, we use the relocated hypocenter with coordinates 19.733°N, 99.689°E at 5 km depth where the aftershocks exists along both the NSTA and the EWTA (Pananont et al. 2017). The sensitivity of the assumption of the model domain depth has been evaluated by testing with alternative depths at 4 km and 6 km (see Stability of the solution subsection), and we find that the fault geometry and rupturing paths are robustly resolved.

4 Numerical test

We perform a numerical test using synthetic waveforms to evaluate a resolvability of our approach for multiplicity of the source process involving the geometric change of the fault system of the smaller-scale earthquake. The synthetic rupture process is assumed to take place along the purely vertical fault planes of two different faults: Faults 1 and 2 (Fig. 4). We generate the synthetic waveforms at 25

teleseismic stations (Fig. 3b), which are the same stations that we use for the analyses of the 2014 Thailand earthquake. Each fault model consists of a set of 1×1 km^2 sub-fault grids situated along the strike and the dip. The total fault length for Fault 1 is 10 km and for Fault 2 is 20 km; the width of both faults is 8 km. The input source model is composed of a spatially variable slip distribution along the strike and is symmetrically distributed centered at depth of the hypocenter along the dip (Fig. 5a). The input total seismic moment is 0.76×10^{19} N m (M_W 6.5). We assume that the rupture initiates at the hypocenter on Fault 1. Then, the rupture front propagates unilaterally toward south along Fault 1 at a constant speed of 3.6 km/s (Fig. 5e). The rupture on Fault 2 initiates at its eastern edge at 1.0 s hypocentral time and propagates unilaterally toward the southwest (Fig. 5e) at a constant speed of 3.6 km/s. We generate the synthetic waveform by using Green's function incorporating Gaussian noise and then adding the background Gaussian noise (Additional file 1: Fig. S8). Then, we invert the synthetic waveforms using the potency density tensor inversion method adopted in this study. The numerical experiment is performed in the same setting of the 2014 Thailand earthquake analysis. The model plane is a non-rectangular horizontal model plane covering the input sources, and the depth of the model plane, 5 km, corresponds to the potency centroid depth of the input model (Fig. 4). The output total seismic moment is 0.75×10^{19} N m (M_W 6.5). The moment rate function (Fig. 5d) is consistent with that of the input (Fig. 5b) and shows minor moment release at ~ 2 s and main moment release at 4–6 s. The resolved spatiotemporal rupture evolution shows that the rupture originates at the hypocenter and propagates southwards along Fault 1 during the first second. Then, a rupture occurs on the east end of Fault 2 and propagates in the southwest direction (Fig. 5f). Although the rupture regions obtained in each time window tend to

Fig. 4 The 3D view of the input and assumed model geometries. The rectangles are the input fault planes (Fault 1 and Fault 2). The dashed polygon is the assumed horizontal model plane for the potency density tensor inversion. The star shows the initial rupture point. The shadow gray solid line, dotted line, and star are map views of the input and inversion model settings

be smoother, the focal mechanisms at each time window are consistent with the fault geometry of the input faults. To confirm the validity of our method, we also conducted numerical tests with two other input models and confirmed that the solution features are reproduced (Additional file 1: Figs. S9 and S10). Overall, the spatiotemporal distribution of the potency-rate density tensor agrees with that of the assigned input model. The results of this numerical test show that, under the present conditions, the potency density tensor inversion can resolve complex ruptures even for cases of smaller-scale events consisting of multiple rupture segments and with geometric changes in the fault system.

5 Results

The total moment tensor solution, calculated by the integration of all potency-rate density tensors, exhibits strike-slip faulting with the two nodal planes striking at 250° (ENE-WSW) and 340° (NNW-SSE) (Fig. 6a). The moment rate function shows at least two rupture episodes: one during 0–2.0 s and the other during 2.0–4.5 s. The highest moment rate occurs at around 3.5 s (Fig. 6b). The total seismic moment is 0.30×10^{19} N m (M_W 6.2), which is larger than the GCMT solution 0.23×10^{19} N m (M_W 6.2). The larger seismic moment in our work is probably due to our model covering a wider area that includes the aftershock distribution along the NSTA and EWTA.

The static distribution of the potency density reveals two large potency zones located in the middle of the EWTA and the NSTA. The larger potency density in the middle of the EWTA is around 1.3 m, and the potency density in the NSTA near the epicenter is around 1.1 m (Fig. 6c). One of the nodal plane distributions of the potency density tensor shows that the strike orientation is at NNE-SSW along the NSTA and at ENE-WSW along the EWTA (Fig. 6c).

The P-axis in Fig. 7 is calculated from the potency density tensor at each sub-fault along the model plane (Fig. 6). The P-axis azimuth distribution exhibits two distinct orientations at ENE-WSW in the middle of the NSTA and at NNE-SSW in the middle of the EWTA (Fig. 7). The P-axis azimuth histogram shows the twin peaks at 20° and 50° (measured clockwise from north), where the first peak of the P-axis azimuth ($\sim 20°$) corresponds to the ones in the EWTA, whereas the second peak ($\sim 50°$) is from the NSTA's (Fig. 7).

The spatiotemporal distribution of the potency-rate density exhibits two rupture episodes, one along the NSTA and the other along the EWTA (Fig. 8a). The initial rupture of the mainshock originates at the hypocenter in the first 1.5 s and propagates south along the NSTA. The second rupture occurs at the eastern edge of the EWTA
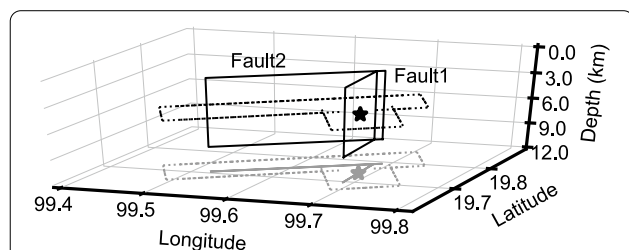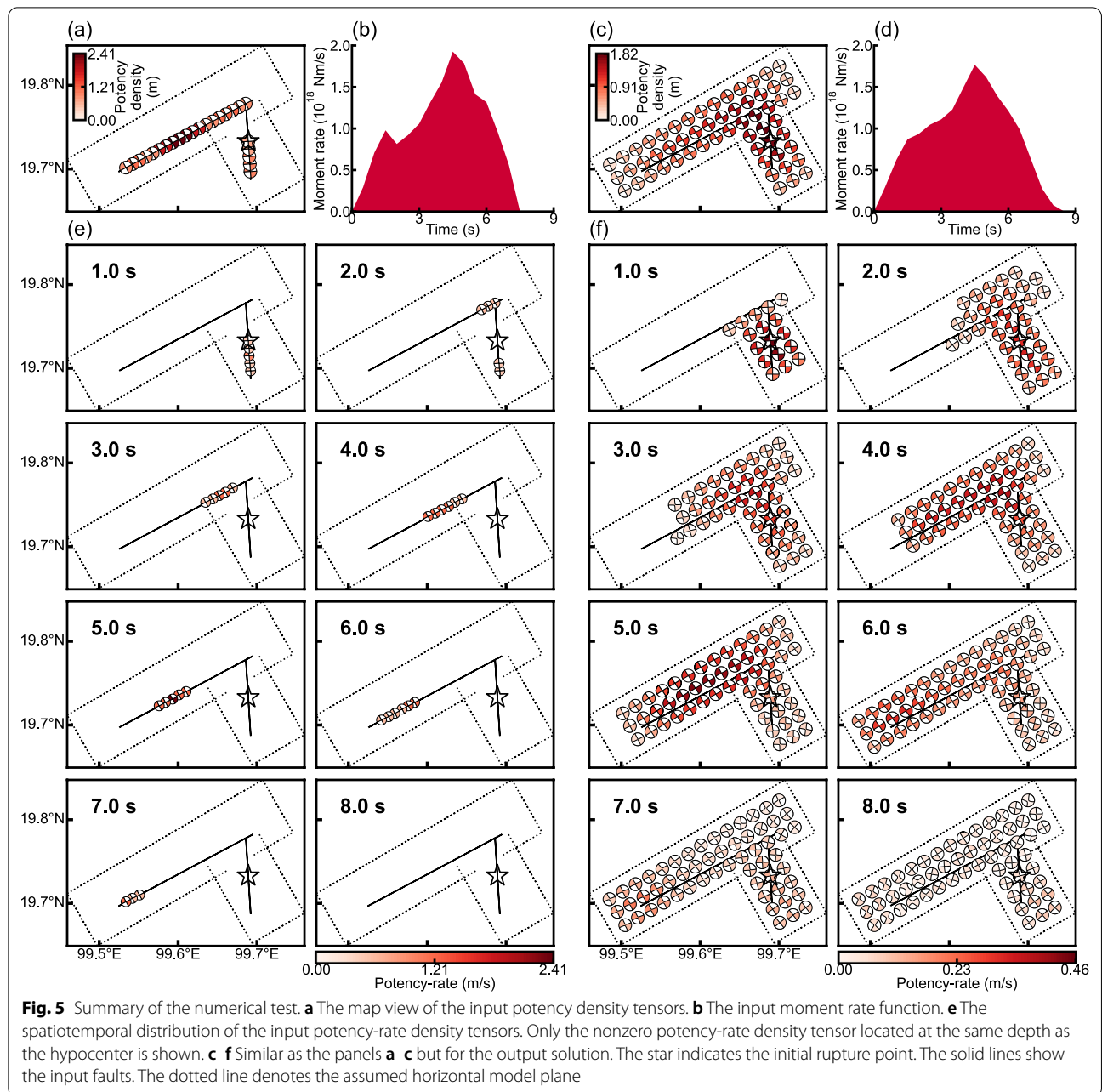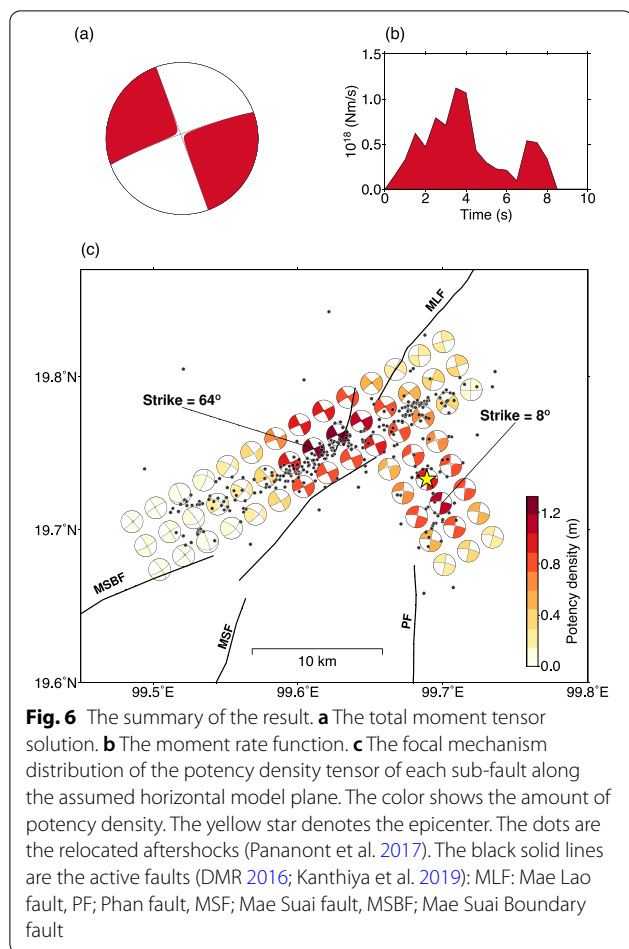
Fig. 5 Summary of the numerical test. **a** The map view of the input potency density tensors. **b** The input moment rate function. **e** The spatiotemporal distribution of the input potency-rate density tensors. Only the nonzero potency-rate density tensor located at the same depth as the hypocenter is shown. **c**–**f** Similar as the panels **a**–**c** but for the output solution. The star indicates the initial rupture point. The solid lines show the input faults. The dotted line denotes the assumed horizontal model plane

between 1.0 s and 1.5 s and propagates southwest along the EWTA (Fig. 8a). The second rupture has the highest potency rate in the middle of the EWTA between 2.0 and 3.0 s and terminates at the west end of the EWTA at 5.0 s. These two rupture episodes coincide with the dominant peaks seen in the moment rate function (Fig. 6). The spatiotemporal distribution of the moment tensor solution shows two dominant patterns of strike-slip faulting (Fig. 8b): one with a strike at NNE-SSW near the epicenter occurred between 0.5 and 1.5 s and the other

with a strike at ENE-WSW northwest from the epicenter occurred between 1.5 and 4.0 s.

6 Discussion
6.1 Stability of the solution
In this study, the horizontal model plane has been set at hypocenter at 5 km depth, even though an actual fault rupture propagates not only horizontal but also in the depth direction. The results of the numerical experiment show that we can estimate the complex rupture processes

Fig. 6 The summary of the result. **a** The total moment tensor solution. **b** The moment rate function. **c** The focal mechanism distribution of the potency density tensor of each sub-fault along the assumed horizontal model plane. The color shows the amount of potency density. The yellow star denotes the epicenter. The dots are the relocated aftershocks (Pananont et al. 2017). The black solid lines are the active faults (DMR 2016; Kanthiya et al. 2019): MLF: Mae Lao fault, PF; Phan fault, MSF; Mae Suai fault, MSBF; Mae Suai Boundary fault

Fig. 7 The P-axis azimuth distribution. **a** The P-axis azimuth distribution extracted from the resultant potency density tensors of each sub-fault from Fig. 6. The length of the P-axis is proportional to the potency density relating to the color scale of Fig. 6. The azimuth is measured clockwise from north. The yellow star shows the epicenter. The dots show the relocated aftershock (Pananont et al. 2017). The black thin line shows the active faults (DMR 2016; Kanthiya et al. 2019). **b** The histogram of the P-axis azimuth, counting the ones corresponding to the larger potency density than 25% of the maximum potency density every 10° azimuthal bin

of the two fault planes by assuming a horizontal model plane at the potency centroid depth. In order to evaluate the modeling sensitivity to the assumption of model domain depth, we tested alternative assumptions of the model plane depth at 4 km and 6 km. The moment rate functions show different peaks among the alternative solutions. The timing of the dominant peak of the moment rate is shifted from 4 to 3 s from shallower to deeper hypocentral models (Additional file 1: Fig. S11). The spatiotemporal distribution of the potency-rate density distributions also shows the time shift of the largest potency-rate release at middle of the EWTA from 3.0 to 2.5 s from shallower to deeper models. These time differences can be explained by the change in the Green's function, which is mainly caused by the difference of model domain depths (e.g., Shimizu et al. 2020). However, the potency density tensor distributions remain the same among the alternative solutions. They show the strike orientations at NNE-SSW and ENE-WSW in the middle of the NSTA and EWTA, respectively (Additional file 1: Fig. S11), which are the same features as seen in our potency density tensor solution. The alternative solutions also
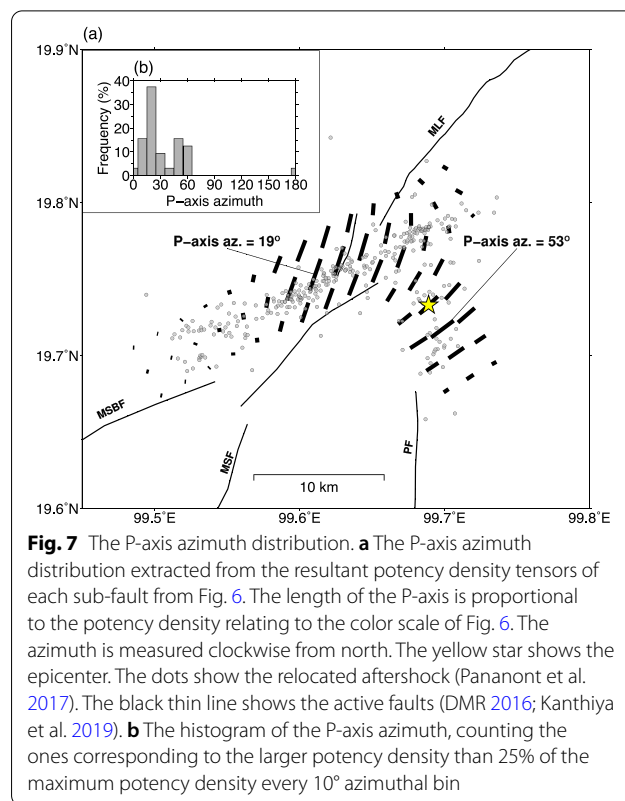
show that the rupturing paths remain the same as our preferred solution; the first rupture propagates toward south along the NSTA, and then the secondary rupture initiates at the eastern edge of the EWTA and propagates toward southwest along the EWTA. The sensitivity tests suggest that, although the rupture timing can be uncertain within ~ 1 s due to the model domain depth, the overall pattern of the rupture episodes is robustly resolved by our modeling approach. We note that estimates of rupture velocity from the potency-rate density tensor solution can inherently be difficult primarily due to smoothing effects applied in both space and time, especially for the smaller-scale earthquake like the 2014 Thailand earthquake, which might be challenging to rigorously resolve the exact timing and location of rupture front.

To further evaluate a reproducibility of the results, we performed the reproduction test by using the solution from our potency density tensor inversion. We generated the synthetic waveforms from our solution and newly performed the inversion (Additional file 1: Fig. S12). The input synthetic waveforms for the reproduction test are generated using the Green's function incorporating Gaussian noise and the background Gaussian noise. Then, we inverted the synthetic waveforms with the same model setting as for our preferred potency density tensor
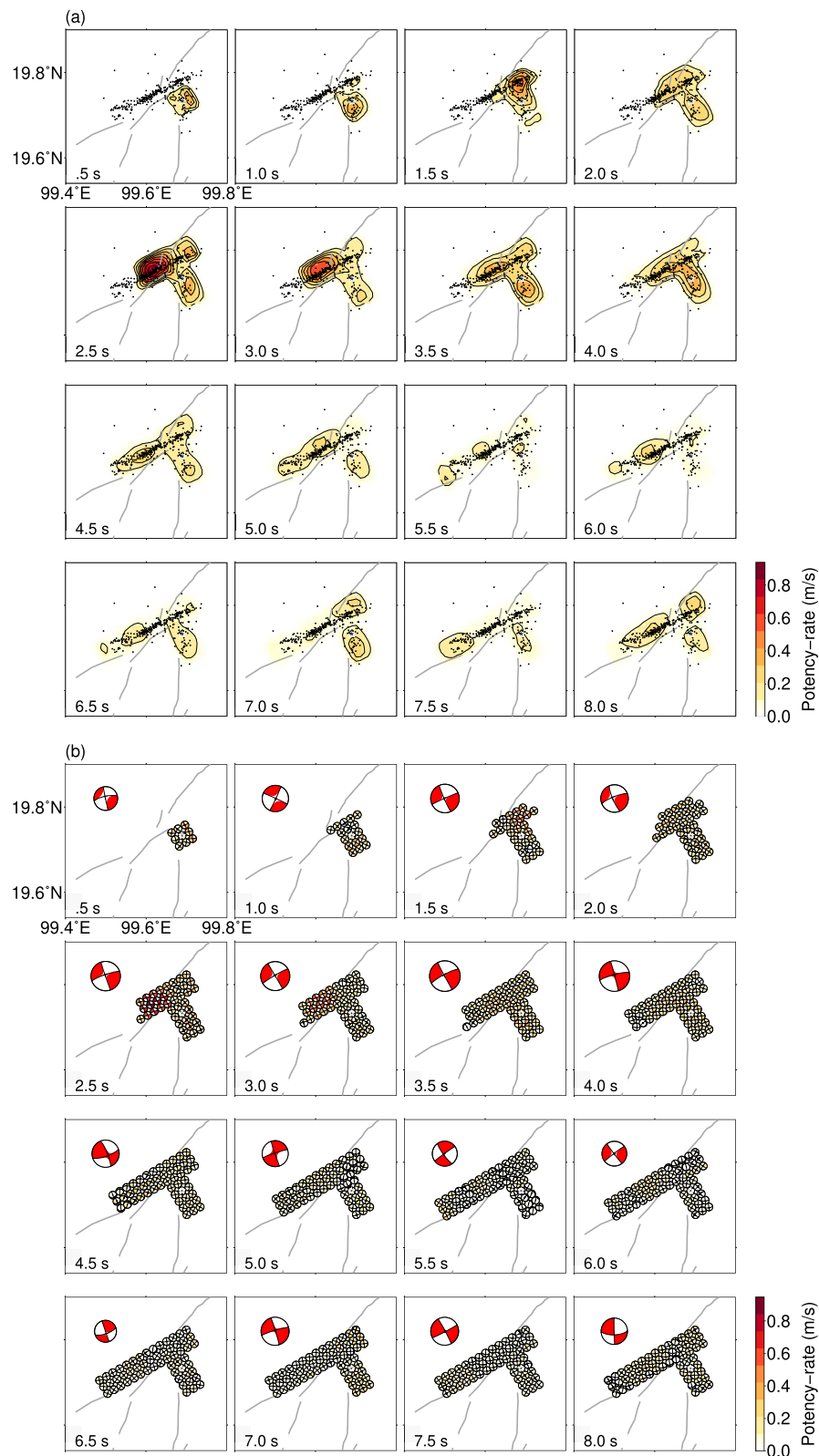
Fig. 8 The spatiotemporal distribution of the **a** potency-rate density and the **b** focal mechanism distribution of the potency-rate density tensor in each time window. The red beach ball shows the total moment tensor solution within the time window. The star shows the epicenter. The dots show the relocated aftershock (Pananont et al. 2017). The line shows the active faults (DMR 2016; Kanthiya et al. 2019)

inversion for the 2014 Thailand earthquake. The result shows that the moment rate function has the major peak at about 3–4 s (Additional file 1: Fig. S12b), which is the same feature as we resolved for our solution (Additional file 1: Fig. S12a). The distribution of the potency density tensor shows that the strike orientations at NNE-SSW and ENE-WSW in the middle of the NSTA and EWTA, respectively, which are the same features as seen in our solution. In addition, the spatiotemporal distribution of the potency-rate density tensor (Additional file 1: Fig. S12d) exhibits two distinct rupture propagation: (1) southward rupture propagation during 0–1.5 s along the NSTA and (2) southwestern rupture propagation during 1.5–4.5 s along the EWTA, which are the main rupture features resolved in our solution (Additional file 1: Fig. S12c), and thus we will focus on these rupture processes in the Discussion section and will avoid discussing detailed features of rupture processes that are not reproduced in the reproduction test.

6.2 Two rupture episodes

Our source model of the 2014 Thailand earthquake distinguished two rupture episodes that show a dominant strike-slip faulting consisting of different rupture lineation along the NSTA and EWTA (Fig. 8), which are consistent with the nodal plane distribution (Fig. 6c) and thus facilitate identification of the possible fault geometry for the 2014 Thailand earthquake. The nodal plane distribution along the NSTA shows nodal strikes in the NNE-SSW direction and the auxiliary plane in the ESE-WNW direction (Fig. 6). The nodal plane distribution along the EWTA shows nodal strikes in the ENE-WSW direction and the auxiliary plane in the NNW-SSE direction (Fig. 6). The consistency between the nodal plane distribution (Fig. 6c) and the rupture directions of the spatiotemporal potency-rate density distribution (Fig. 8) helps facilitate identification of the possible fault geometry. The striking plane along the NSTA is determined to be in the NNE-SSW direction and is associated with the rupture propagating toward the south. The striking plane along the EWTA is determined to be in the ENE-WSW direction and is associated with the rupture propagating toward the southwest. The obtained two dominant fault planes along the NSTA and EWTA are consistent with the two distinct trends of the relocated aftershock distribution (Pananont et al. 2017). The first is the N-S trend (~180° from north) along the NSTA located near the epicenter, and the second is the ENE-WSW trend (~60° from north) along the EWTA located northwest from the epicenter. Although the geometry of our model, designed to cover the aftershock distribution area, is non-rectangular, the potency density and the potency-rate density

of each sub-fault are estimated independently from the assumed model geometry.

During the first 1.5 s, the rupture propagates from the hypocenter to the southern edges of the NSTA (Fig. 8b). Then, at around 1.5 s as the rupture migrates from the NSTA to the EWTA, the fault strike direction changes from NNE-SSW at the northern edge of the NSTA to ENE-WSW at the eastern edge of the EWTA, which implies that the fault planes in the NSTA and EWTA can be considered as a conjugate fault, where the planes inclined at angles on either side of the maximum principal stress (Scholz 2002). Next, between 2.0 and 3.5 s the second rupture propagates along EWTA from its eastern edge toward the southwest and terminates at around 5.0 s at its western edge. It is associated with the second rupture arising at the eastern edge of the EWTA, propagating west during the period between the 2.0 and 3.5 s and having the highest potency-rate of around 0.9 m/s (Fig. 8b). Our result of the major slip along the EWTA is robustly resolved even if we change the near-source structure model, the assumptions of the total duration, and the maximum rupture velocity (Additional file 1: Figs. S4, S6, and S7). According to the surface fault lines (DMR 2016; Noisagool et al. 2016), the orientation of the known active conjugated strike-slip faults of the PF and MLF shows striking at N5°E–N13°E and N30°E–N50°E; this is consistent with our findings that at the northern edge of the NSTA, the striking is in the NNE-SSW direction and at the eastern edge of the EWTA, in the ENE–WSW direction. The multiple subevents at the conjugated strike-slip fault system are possibly due to the complex rupture evolution among the geometrically complex fault system (e.g., Meng et al. 2012; Yamashita et al. 2021). Therefore, our solution suggests that the rupture evolution of the 2014 Thailand earthquake is characterized by multiple subevents in the conjugated strike-slip fault system of the PF and MLF.

Our results indicate that the conjugate fault ruptured during the mainshock, but Pananont et al. (2017) suggests that primary rupture on the N-S trending fault plane during the mainshock may host the aftershock activity triggered on the conjugate structure of the ENE-WSW trending fault plane. Therefore, we examined whether the observed waveforms could be explained if the rupture occurred only on the N-S trending fault. We first set up a single fault plane with reference to the north–south-striking nodal plane of the focal mechanism obtained in Pananont et al. (2017) and inverted the observed waveforms on that plane using the finite-fault inversion method (Yagi and Fukahata 2011), assuming a two-component basis slip vector (Additional file 1: Fig. S13). As a result, the variance reduction (Shimizu et al. 2021) decreases significantly from 73% to 54% (Additional file 1:

Fig. S14), indicating that the model with no variation in fault geometry cannot explain the complex teleseismic waves of the present earthquake. We next performed the potency density tensor inversion (the adopted method in this study), placing the horizontal model plane only on the NSTA (Additional file 1: Fig. S15). The potency density tensor inversion projects the slips on multiple faults onto the assumed model plane. Therefore, if a large seismic potency is released on the ENE-WSW trending fault, it is expected that subevents corresponding to the ENE-WSW trending fault slip will be detected near the model plane boundaries and that the waveforms will be poorly fitted due to the improper model plane. As expected, the obtained results of the spatial distribution and the spatiotemporal distribution (Additional file 1: Fig. S15) show that subevents with focal mechanisms corresponding to slip on the ENE-WSW trending fault are projected on the northwest boundary of the assumed model plane and with a variance reduction of 66% (Additional file 1: Fig. S14). These two results indicate that a model in which two faults rupture during the mainshock is necessary to explain the complex teleseismic body waves.

6.3 P-axis distribution

The spatial distribution of the P-axis azimuth, extracted from the potency density tensor for each sub-fault, exhibits two major orientations at ENE-WSW in the NSTA and NNE-SSW in the EWTA (Fig. 7). The histogram of the P-axis azimuth distribution displays two peaks, one at 20°–30° and the other at 50°–60° (Fig. 7b), which should reflect the dominant orientations within the EWTA and NSTA, respectively. Our P-axis orientations at 20°–30° within the EWTA are consistent with the one obtained by Noisagool et al. (2016), which is estimated based on the mainshock and aftershocks focal mechanisms, mostly located within the EWTA (Pananont et al. 2017), while the direction of our P-axis azimuth along the NSTA obtained in this study ($\sim$50°, Fig. 7) is not consistent with the one ($\sim$18°) obtained by Noisagool et al. (2016). However, if Coulomb's friction factor is a typical value of 0.6, the two peaks of our P-axis histogram (Fig. 7) can be naturally explained as a shift of the P-axis of the conjugate fault plane (Iio 1997), which leads to $\sim$35°. We should mention, however, the focal mechanism solutions obtained in this study are affected by dynamic changes in the stress field due to seismic waves or localized fault structures, and estimation of the principal stress axis is beyond the scope of this study. Our results suggest that further investigation of the stress field in this region is needed, taking into account the spatial bias of aftershock distribution, which affects the estimates of the principal stresses for the conjugate fault earthquake.

7 Conclusion

We construct a source model for the 2014 Thailand M_W 6.2 earthquake that occurred within the Phayao Fault Zone in northern Thailand, by applying a new framework of the potency density tensor inversion and resolved both the fault geometry and the slip. Our source model exhibits complex rupture evolution consisting of two rupture episodes along a conjugated strike-slip fault system that comprises two distinct fault planes. These planes coincide with the relocated aftershock distribution. The initial rupture originates at the hypocenter and propagates southward along the north–south oriented fault plane near the epicenter. Then, the second rupture episode is triggered north of the epicenter at the eastern edge of the conjugated east–west oriented fault plane and propagates southwestward until the rupture terminates. The teleseismic waveform shape can be modulated by the focal mechanism changes during the rupture propagation along the geometrically complex fault system. Especially for the case of the 2014 Thailand earthquake, the rupture along the different mechanisms of the two distinct conjugate faults generates different shape of the teleseismic waves accordingly. Such information of the fault geometry change included in the teleseismic data is properly retrieved by our approach of the potency density tensor inversion (Shimizu et al. 2020), leading to resolving the complex rupture evolution associated with the complex fault geometry, even for the smaller-scale *M*6-class earthquakes.

Abbreviations
PFZ: Phayao Fault Zone; MLF: Mae Lao fault; PF: Phan fault; NSTA: N-S trending aftershock; EWTA: ENE-WSW trending aftershock; MSF: Mae Suai fault; MSBF: Mae Suai boundary fault; Az: Azimuth; Del: Epicentral distance; ABIC: Akaike's Bayesian information criterion.

Supplementary Information

Additional file 1: Text S1. Uncertainty and sensitivity analyses of the potency density tensor inversion. **Figure S1.** The summary of the relative weight smoothness constraint for each basis moment tensor component from M1 to M5 (Kikuchi and Kanamori 1991). **Figure S2.** The comparison of the results adopting the different weight smoothness constraints of 5%, 10% and 20% of the maximum relative standard deviation. **Figure S3.** The waveform fitting between the observed waveform and the synthetic waveform of the 2014 Thailand earthquake. **Figure S4.** The summary of the sensitivity test of the near-source structure models using the CRUST1.0 model (Laske et al. 2013) (Additional file 1: Table S2) and the regional velocity model (Wongwai et al. 2013) (Additional file 1: Table S1). **Figure S5.** An impulse response function of the effect of inelastic attenuation of the Earth. **Figure S6.** The summary of the sensitivity test of the total rupture duration assumption at 6 s, 8 s, 10 s, and 12 s. **Figure S7.** The summary of the sensitivity test of the maximum rupture velocity assumption at 3.2 km/s, 3.6 km/s, and 4.0 km/s. **Figure S8.** The waveform fitting between the input and output waveforms from the numerical test (Figs. 4 and 5). **Figure S9.** Summary of the numerical test of the input of

Tadapansawut *et al. Progress in Earth and Planetary Science*   (2022) 9:26

Page 12 of 13

rupture propagating toward NE along Fault 2. **Figure S10.** Summary of the numerical test of one input rupture fault of the Fault 1. **Figure S11.** The summary of the sensitivity test of the different model plane depth at 4 km, 5 km, and 6 km. **Figure S12.** The summary of the reproduction test. **Figure S13.** The summary of a single vertical fault plane analysis. **Figure S14.** The waveform fit between the observed waveform and the synthetic waveform of our study, an assumed horizontal plane covering only on the N-S analysis in Additional file 1: Fig. S15, and a single vertical mode plane analysis in Additional file 1: Fig. S13. **Figure S15.** The summary of the analysis assuming a horizontal model plane covering only the N-S segment. **Table S1.** Velocity structure (Wongwai et al. 2013) used for calculating Green's function. **Table S2.** Velocity structure used for calculating Green's function made from CRUST1.0 model (Laske et al. 2013).

Author contributions
YY and TT conceptualized the study. TT, YY, KS, and SY developed the methodology. TT, YY, KS, and SY performed data analyses. TT, SY, and RO visualized the data. YY supervised the study and acquired the fund. TT wrote the original draft. All authors validated the results and read and approved the final manuscript.

Availability of data and materials
Teleseismic waveforms were obtained from the following networks: the Global Seismograph Network (GSN IRIS/IDA, II; https://doi.org/10.7914/SN/II); the Global Seismograph Network (GSN IRIS/USGS, IU; https://doi.org/10.7914/SN/IU); New China Digital Seismograph Network (NCDSN, IC; https://doi.org/10.7914/SN/IC); the Alaska Regional Network (AK; https://doi.org/10.7914/SN/AK); the Australian National Seismograph Network (ANSN, AU; http://www.fdsn.org/networks/detail/AU/); the China National Seismic Network, the Data Management Centre of the China National Seismic Network at the Institute of Geophysics (SeisDmc CEA, CB; https://doi.org/10.7914/SN/CB); the Czech Regional Seismic Network (CZ; https://doi.org/10.7914/SN/CZ); GEOFON (GE; https://doi.org/10.14470/TR560404); the Japan Meteorological Agency Seismic Network (JP; http://www.fdsn.org/networks/detail/JP/); the Kyrgyz Seismic Telemetry Network (KNET, KN; https://doi.org/10.7914/SN/KN); the Mediterranean Very Broadband Seismographic Network (MedNet, MN; https://doi.org/10.13127/SD/fBBBtDtd6q); and the Austrian Seismic Network (OE; https://doi.org/10.7914/SN/OE). The moment tensor solutions were obtained from the GCMT catalog (https://www.globalcmt.org/CMTsearch.html). The CRUST 1.0 structural velocity model of Laske et al. (2013) is available at https://igppweb.ucsd.edu/~gabi/crust1.html. The topography and bathymetry data from SRTM15+are available at https://topex.ucsd.edu/pub/srtm15_plus/. The global database of the major active faults from Styron and Pagani (2020) is available at https://github.com/GEMScienceTools/gem-global-active-faults.

Declarations

Competing interests
The authors declare that they have no competing interests.

Author details
[1]Graduate School of Life and Environmental Sciences, University of Tsukuba, Tsukuba, Ibaraki 305-8572, Japan. [2]Faculty of Life and Environmental Sciences, University of Tsukuba, Tsukuba, Ibaraki 305-8572, Japan. [3]Mountain Science Center, University of Tsukuba, Tsukuba, Ibaraki 305-8572, Japan. [4]COMET, School of Earth and Environment, University of Leeds, Leeds LS2 9JT, UK. [5]Graduate School of Science and Technology, University of Tsukuba, Tsukuba, Ibaraki 305-8572, Japan.

References
Akaike H (1980) Likelihood and the Bayes procedure. Trabajos De Estadistica Y De Investigacion Operativa 31(1):143–166. https://doi.org/10.1007/BF02888350

Beyreuther M, Barsch R, Krischer L, Megies T, Behr Y, Wassermann J (2010) ObsPy: a python toolbox for seismology. Seismol Res Lett 81(3):530–533. https://doi.org/10.1785/gssrl.81.3.530

Bird P (2003) An updated digital model of plate boundaries. Geochem Geophys. https://doi.org/10.1029/2001GC000252

Charusiri P, Pum-Im S (2009) Cenozoic tectonic evolution of major sedimentary Basins in Central, Northern, and the Gulf of Thailand. Best 2(2):40–62

DeMets C, Gordon RG, Argus DF (2010) Geologically current plate motions. Geophys J Int 181(1):1–80. https://doi.org/10.1111/j.1365-246X.2009.04491.x

DMR Department of Mineral Resources (2016) Active fault map of Thailand. Retrieved from http://www.dmr.go.th/n_more_news_en.php?nid=109490

Duputel Z, Agram PS, Simons M, Minson SE, Beck JL (2014) Accounting for prediction uncertainty when inferring subsurface fault slip. Geophys J Int 197(1):464–482. https://doi.org/10.1093/gji/ggt517

Dziewonski AM, Chou TA, Woodhouse JH (1981) Determination of earthquake source parameters from waveform data for studies of global and regional seismicity. J Geophys Res 86(B4):2825–2852. https://doi.org/10.1029/JB086iB04p02825

Ekström G, Nettles M, Dziewoński AM (2012) The global CMT project 2004–2010: centroid-moment tensors for 13,017 earthquakes. Phys Earth Planet Inter 200–201:1–9. https://doi.org/10.1016/j.pepi.2012.04.002

Fenton CH, Charusiri P, Wood SH (2003) Recent paleoseismic investigations in Northern and Western Thailand. Ann Geophys 46(5):957–982. https://doi.org/10.4401/ag-3464

Fukahata Y, Wright TJ (2008) A non-linear geodetic data inversion using ABIC for slip distribution on a fault with an unknown dip angle. Geophys J Int 173(2):353–364. https://doi.org/10.1111/j.1365-246X.2007.03713.x

GCMT (2014) Mw 6.2 Chiang Rai, Thailand. Retrieved from https://ds.iris.edu/spud/momenttensor/9687293

Heidbach O, Rajabi M, Reiter K, Ziegler M, WSM Team (2016) World stress map database release 2016. V. 1.1. (GFZ data services). https://doi.org/10.5880/WSM.2016.001

Huchon P, Le Pichon X, Rangin C (1994) Indochina Peninsula and the collision of India and Eurasia. Geology 22(1):27–30. https://doi.org/10.1130/0091-7613(1994)022%3c0027:IPATCO%3e2.3.CO;2

Hunter JD (2007) Matplotlib: a 2D graphics environment. Comput Sci Eng 9(3):90–95. https://doi.org/10.1109/MCSE.2007.55

Iio Y (1997) Frictional coefficient on faults in a seismogenic region inferred from earthquake mechanism solutions. J Geophys Res Solid Earth 102(B3):5403–5412. https://doi.org/10.1029/96jb03593

ISC (2021) International seismological centre. https://doi.org/10.31905/D808B830

Kanthiya S, Mangkhemthong N, Morley CK (2019) Structural interpretation of Mae Suai Basin, Chiang Rai Province, based on gravity data analysis and

modelling. Heliyon 5(2):e01232. https://doi.org/10.1016/j.heliyon.2019.e01232

Kázmér M, Sanittham K, Charusiri P, Pailoplee S (2011) Archaeoseismology of the AD 1545 Earthquake in Chiang Mai Thailand. In: 2nd INQUA-IGCP-567 international workshop on active tectonics, earthquake geology, archaeology and engineering, Corinth, Greece, 1–4. Retrieved from http://www.eatgru.sc.chula.ac.th/Thai/research/pdf/paper_2/111.pdf

Kikuchi M, Kanamori H (1991) Inversion of complex body waves-III. BSSA 81(6):2335–2350. https://doi.org/10.1785/BSSA0810062335

Laske G, Masters G, Ma Z, Pasyanos M (2013) Update on CRUST1.0–A 1-degree global model of earth's crust. Geophys Res Abs 15:2658

Leloup PH, Amaud N, Lacassin R, Kienast JR, Harrison TM, Phantrong TT, Replumaz A, Tapponnier P (2001) New constraints on the structure, thermochronology, and timing of the Ailao Shan-Red River shear zone, SE Asia. J Geophys Res 106:6683–6732. https://doi.org/10.1029/2000JB900322

Lhamphoonsup K, Soisa T, Sriwangpon P (2014) Preliminary geophysical investigation in an earthquake impact area Chiang Rai Province. In: Annual meeting report of the 2014 Chiang Rai earthquake. Retrieved from http://www.dmr.go.th/download/article/article_2014111915 1717.pdf

Meng L, Ampuero JP, Stock J, Duputel Z, Luo Y, Tsai VC (2012) Earthquake in a maze: compressional rupture branching during the 2012 Mw 8.6 Sumatra earthquake. Science 337(6095):724–726. https://doi.org/10.1126/science.1224030

Morley CK (2002) A tectonic model for the tertiary evolution of strike-slip faults and rift basins in SE Asia. Tectonophysics 347(4):189–215. https://doi.org/10.1016/S0040-1951(02)00061-6

Morley CK (2007) Variations in Late Cenozoic-Recent strike-slip and oblique-extensional geometries, within Indochina: the influence of pre-existing fabrics. J Struct Geol 29(1):36–58. https://doi.org/10.1016/j.jsg.2006.07.003

Morley CK, Charusiri P, Watkinson IM (2011) Structural geology of Thailand during the Cenozoic. In: Ridd MF, Barber AJ, Crow MJ (eds) The geology of Thailand. The Geological Society of London, pp 273–334. https://doi.org/10.1144/GOTH.11

Nardkulpat A, Phodee P, Karnchanasuthum S, Nualchawee K, Rakwatin P (2017) Using differential InSAR technique for coseismic displacement study of Mw6.3 Chiang Rai earthquake, Thailand. In: Conference: GEOINFOTECH2017. Retrieved from http://research.gistda.or.th/assets/uploads/pdfs/49784-7.-differential-insar-mw-6.3-.pdf

Noisagool S, Boonchaisuk S, Pornsopin P, Siripunvaraporn W (2016) The regional moment tensor of the 5 May 2014 Chiang Rai earthquake (Mw = 6.5), Northern Thailand, with its aftershocks and its implication to the stress and the instability of the Phayao Fault Zone. J Asian Earth Sci 127:231–245. https://doi.org/10.1016/j.jseaes.2016.06.008

Pailoplee S, Charusiri P (2016) Seismic hazards in Thailand: a compilation and updated probabilistic analysis. Earth Planet Sp 68:98. https://doi.org/10.1186/s40623-016-0465-6

Pailoplee S, Sugiya Y, Charusiri P (2009) Determini s tic and probabili stic seismic hazard analyses in Thailand and adjacent areas using active fault data. Earth Planet Sp 61:1313–1325. https://doi.org/10.1186/BF03352984

Pananont P, Herman MW, Pornsopin P, Furlong KP, Habangkaem S, Waldhauser F, Wongwai W, Limpisawas S, Warnitchai P, Kosuwan S, Wechbunthung B (2017) Seismotectonics of the 2014 Chiang Rai, Thailand, earthquake sequence. J Geophys Res: Solid Earth 122(8):6367–6388. https://doi.org/10.1002/2017JB014085

Ragon T, Sladen A, Simons M (2018) Accounting for uncertain fault geometry in earthquake source inversions - I: theory and simplified application. Geophys J Int 214(2):1174–1190. https://doi.org/10.1093/gji/ggy187

Scholz CH (2002) The Mechanics of earthquakes and faulting. Cambridge University Press. https://doi.org/10.1017/CBO9780511818516

Shimizu K, Yagi Y, Okuwaki R, Fukahata Y (2020) Development of an inversion method to extract information on fault geometry from teleseismic data. Geophys J Int 220(2):1055–1065. https://doi.org/10.1093/gji/ggz496

Shimizu K, Yagi Y, Okuwaki R, Fukahata Y (2021) Construction of fault geometry by finite-fault inversion of teleseismic data. Geophys J Int 224(2):1003–1014. https://doi.org/10.1093/gji/ggaa501

Simons WJF, Socquet A, Vigny C, Ambrosius BAC, Abu SH, Promthong C, Subaya C, Sarsito DC, Matheussen S, Morgan P, Spakman W (2007) A decade of GPS in Southeast Asia: resolving Sundaland motion and boundaries. J Geophys Res Solid Earth 112(6):1–20. https://doi.org/10.1029/2005JB003868

Styron R, Pagani M (2020) The GEM global active faults database. Earthq Spectra 36(1):160–180. https://doi.org/10.1177/8755293020944182

Tadapansawut T, Okuwaki R, Yagi Y, Yamashita S (2021) Rupture process of the 2020 Caribbean earthquake along the Oriente transform fault, involving supershear rupture and geometric complexity of fault. Geophys Res Lett 48(1):1–19. https://doi.org/10.1029/2020GL090899

TMD Thai Meteorological Department (2014) Mw 6.3 Chiang Rai, Thailand. Retrieved from https://earthquake.tmd.go.th/inside-info.html?earthquake=2085

Tozer B, Sandwell DT, Smith WHF, Olson C, Beale JR, Wessel P (2019) Global bathymetry and topography at 15 arc sec: SRTM15+. Earth Space Sci 6(10):1847–1864. https://doi.org/10.1029/2019EA000658

USGS (2014) M6.1 - 13 km NNW of Phan, Thailand. Retrieved from https://earthquake.usgs.gov/earthquakes/eventpage/usb000qack/executive

Wechbunthung B (2014) Seismic data of earthquake at Chaing Rai on May 5, 2014. In: annual meeting report of the 2014 Chiang Rai earthquake. Retrieved from http://www.dmr.go.th/download/article/article_20141 119151717.pdf

Wessel P, Smith WHF, Scharroo R, Luis J, Wobbe F (2013) Generic mapping tools: improved version released. Eos 94(45):409–410. https://doi.org/10.1002/2013EO450001

Wiwegwin W, Kosuwan S (2014) Annual meeting report of the 2014 Chiang Rai earthquake. Retrieved from http://www.dmr.go.th/download/article/article_20141119151717.pdf

Wongwai W, Pananont P, Pornsopin P (2013) Teleseismic receiver functions study of the crustal thickness underneath Thailand. AGU, fall meeting 2013, Abstract Id. S33F-03. Retrieved from http://adsabs.harvard.edu/abs/2013AGUFM.S33F..03W

Yabuki T, Matsu'ura M (1992) Geodetic data inversion using a Bayesian information criterion for spatial distribution of fault slip. Geophys J Int 109(2):363–375. https://doi.org/10.1111/j.1365-246X.1992.tb00102.x

Yagi Y, Fukahata Y (2008) Importance of covariance components in inversion analyses of densely sampled observed data: an application to waveform data inversion for seismic source processes. Geophys J Int 175(1):215–221. https://doi.org/10.1111/j.1365-246X.2008.03884.x

Yagi Y, Fukahata Y (2011) Introduction of uncertainty of Green's function into waveform inversion for seismic source processes. Geophys J Int 186(2):711–720. https://doi.org/10.1111/j.1365-246X.2011.05043.x

Yamashita S, Yagi Y, Okuwaki R, Shimizu K, Agata R, Fukahata Y (2021) Consecutive ruptures on a complex conjugate fault system during the 2018 Gulf of Alaska earthquake. Sci Rep 11(1):1–9. https://doi.org/10.1038/s41598-021-85522-w

Publisher's Note